

Interplay of short-range bond order and A-type antiferromagnetic order in metallic triangular lattice GdZn_3P_3

Jiesen Guo¹, Fan Yang¹, Yuzhou He², Xinyang Liu^{1,2,3}, Zheng Deng^{2,4}, Qinghua Zhang^{2*},
Xiancheng Wang^{2,4}, Xianlei Sheng^{1*}, Wei Li^{3,5,6}, Changqing Jin^{2,4}, and Kan Zhao^{1*}

¹School of Physics, Beihang University, Beijing 100191, China

²Beijing National Laboratory for Condensed Matter Physics,

Institute of Physics, Chinese Academy of Sciences, Beijing 100190, China

³CAS Key Laboratory of Theoretical Physics, Institute of Theoretical Physics, Chinese Academy of Sciences, Beijing 100190, China

⁴School of Physical Sciences, University of Chinese Academy of Sciences, Beijing 100190, China

⁵CAS Center for Excellence in Topological Quantum Computation, University of Chinese Academy of Sciences, Beijing 100190, China

⁶Peng Huanwu Collaborative Center for Research and Education, Beihang University, Beijing 100191, China

*Corresponding author email: zqh@iphy.ac.cn, xlsheng@buaa.edu.cn, kan_zhao@buaa.edu.cn

Abstract:

We investigate a hexagonal ScAl_3C_3 -type antiferromagnet GdZn_3P_3 single crystal. Compared with antiferromagnetic topological material EuM_2X_2 ($\text{M}=\text{Zn}, \text{Cd}$; $\text{X}=\text{P}, \text{As}$), the GdZn_3P_3 features an additional ZnP_3 trigonal planar units. Notably, single-crystal X-ray diffraction analysis reveals that Zn and P atoms within trigonal planar layer exhibit significant anisotropic displacement parameters with a space group of $\text{P6}_3/\text{mmc}$. Meanwhile, scanning transmission electron microscopy experiment demonstrates the presence of interstitial P atoms above and below the ZnP honeycomb lattice, suggesting potential ZnP bond instability within the ZnP_3 trigonal layer. Concerning the triangular Gd^{3+} layer, the magnetic susceptibility $\chi(T)$ and heat capacity measurements reveal long-range antiferromagnetic order at $T_N = 4.5$ K. Below T_N , the in-plane $\chi(T)$ is nearly 4 times the $\chi(T)$ along c axis, indicative of strong magnetic anisotropy. The Curie Weiss fitting to the low temperature $\chi(T)$ data reveals ferromagnetic interaction ($\theta_{cw} = 5.2$ K) in ab -plane, and antiferromagnetic interaction ($\theta_{cw} = -1$ K) along c axis, suggesting the ground state as an A-type antiferromagnetic order. Correspondingly, the density function theory calculation shows that GdZn_3P_3 is an indirect semiconductor with a band gap 0.27 eV, supported by the resistivity measurement on polycrystal sample. Interestingly, the GdZn_3P_3 single crystal exhibits metallic conductivity with an anomaly at T_N , likely associated with the observation of interstitial P atoms mentioned above. Therefore, our results establish GdZn_3P_3 system as a concrete example for investigating the coupling between charge carrier and triangular lattice magnetism in the two-dimensional lattice framework, on the background of short-range bond order.

Introduction:

Geometric frustration in magnetism has long been a prominent research focus in condensed matter physics, as this model prevents antiparallel spin alignment in the antiferromagnetic ground state. This results in significant entanglement and fluctuations, giving rise to many novel states, such as spin liquid [1-8], spin ice [9-16] and spin supersolid [17-20]. As the prototype model of the two-dimensional (2D) triangular lattice formed by rare earth ions has attracted more attention, notable examples include the quantum spin liquid candidate YbMgGaO_4 [3-8] and ARCh_2 (A=alkali or monovalent ions, R=rare earth, and Ch=O, S, Se) [21-24]. While most 2D triangular systems focus on insulators, and the presence of itinerant electrons in the triangular lattice material, the emergence of exotic magnetic order could be driven by the Ruderman–Kittel–Kasuya–Yosida (RKKY) interactions.

Based on the above idea, the hexagonal ScAl_3C_3 -type RM_3X_3 (R=rare earth; M=Zn, Cd; X=P, As) compounds have been widely studied, with $\text{P6}_3/\text{mmc}$ space group [25-29]. As shown in Fig. 1(a), the crystal structure of RM_3X_3 features alternating layers of RX_6 octahedra, MX_4 tetrahedra, and MX_3 trigonal planar units, the M_{trig} and X_{trig} atoms of MX_3 are cross-arranged to form a honeycomb [26]. To compare, the antiferromagnetic topological materials EuM_2X_2 (M=Zn, Cd; X=P, As) crystallize in a trigonal system with the $\text{P}\bar{3}\text{m}1$ (No. 164) space group, constituting by an layered structure composed of edge-sharing MX_4 tetrahedra and EuX_6 octahedra [30-40]. The interlayer distance between the triangular lattice layer of Eu^{2+} & Ce^{3+} ions increases from 7.1683 Å in EuCd_2P_2 and 7.3278 Å in EuCd_2As_2 , to 10.2387 Å in CeCd_3As_3 , which enhances the two-dimensional character of the RM_3X_3 structure. Previous studies of CeCd_3X_3 (X=P, As) have demonstrated strong easy-plane magnetic anisotropy explained by crystalline electric field (CEF) model [41], which demonstrated the low-carrier-density metallic state, with antiferromagnetic (AFM) transition at about 0.4 K [42, 43]. In the $J_{\text{eff}}=1/2$ compound NdCd_3P_3 , the AFM transition temperature of 0.34 K is slightly lower than that of CeCd_3X_3 (X=P, As) [44], as well as this trend of magnetic transition is similar to that of RZn_3P_3 (R=rare earth) [28, 45].

During the structural refinement within $\text{P6}_3/\text{mmc}$ space group, both Cd_{trig} and As_{trig} atoms of CeCd_3As_3 exhibit significantly large displacement parameters [26]. As reported in Ref. [26], this pathological issue can be partially removed by splitting atom positions, or incorporating twins in a low-symmetry space group. Fig.1(a) illustrates an acceptable model that the Cd_{trig} and As_{trig} atoms are shifted from the ideal 2c and 2d sites (with $-6\text{m}2$ symmetry) to 6h sites ($\text{mm}2$ symmetry) at a partial occupancy of 1/3. Within the 6h sites, the 1/3 occupancy indicates the Cd and As atoms are randomly occupied in the three positions, forming a local distorted arrangement within the CdAs_3 trigonal planar layer. The scenario could be treated as a dynamic movement of Cd_{trig} acting on the surrounding As_{trig} atoms, which may cause the bond instability of $(\text{CdAs})_{\text{trig}}$.

Recently, Ref. [46] provides direct evidence of the local distortion of CdP bonds associated with one-dimensional CdP chains in RCd_3P_3 (R=La, Ce, Pr, and Nd) single crystals, based on the observation of diffuse intensity in synchrotron X-ray diffraction measurement. By mapping the Cd-P dimer covering problem onto a 2D Ising model defined on the dual triangular lattice, the effective interactions associated with the local bond order on the honeycomb lattice hinder the development of long-range order [46]. Therefore, the coexistence of bond instability and frustrated magnetism

renders the RCd_3P_3 system particularly intriguing, as it extends the concept of geometrical frustration from solely encompassing the magnetic component of electrons to incorporating both spin and charge degrees of freedom. It is crucial to identify an isostructural compound with a relatively high magnetic transition temperature in order to facilitate the investigation of the interplay between these two frustrated subsystems.

In this paper, we present the synthesis and characterization of iso-structural GdZn_3P_3 single crystal. The ZnP bond instability within ZnP_3 trigonal planar units has been revealed through both single crystal X-ray diffraction and scanning transmission electron microscopy (STEM) experiment. Based on the magnetic and thermodynamic data, we identify the ground state of GdZn_3P_3 as an A-type AFM order below $T_N = 4.5$ K. The GdZn_3P_3 system is calculated to be a semiconductor with a band gap of 0.27 eV by DFT method, consistent with the value of 0.2 eV extracted from polycrystalline resistivity data. During single crystal growth, the presence of interstitial P atoms would cause hole-doping into the GdZn_3P_3 system, inducing the metallic conductivity with an anomaly at T_N . Thus, the metallic GdZn_3P_3 single crystal gives rise to the unique opportunity of investigating the emergent phenomenon in antiferromagnetic RM_3X_3 system, such as the topological hall effect related with the unconventional spin texture, as well as the charge carrier induced superconductivity.

Experimental:

The polycrystals of CeCd_3As_3 and GdZn_3P_3 were synthesized by solid-state method. The CdAs, CdP, and ZnP precursors were first weighed in a glove box using a stoichiometric ratio of Cd powder (99.99%), As lump (99.99%), P lump (99.99%) and Zn powder (99.99%), then mixed in an agate mortar and sealed in an evacuated quartz tube. CdAs was sintered at 500 °C for 30 h, and CdP and ZnP were sintered at 250 °C for 30 h. CdAs and Ce (99.99%), CdP and Gd (99.99%), and ZnP and Gd were mixed at stoichiometric ratios and sintered. As shown in Fig. S1-S2 [47], the phase pure CeCd_3As_3 and GdZn_3P_3 polycrystals have been successfully obtained under sintering at 700 °C for 30 h and 1100 °C for 30 h. High-quality single crystals of GdZn_3P_3 were grown by 0.5 g of stoichiometric amounts of Gd lump (99.99%), Zn powder (99.99%), and P lump (99.99%) together with 4 g of the NaCl/KCl (1:1) flux [25, 28]. The sample was annealed for 24 h at 500 °C, followed by 170 h at 900 °C, then furnace cool to room temperature. The plate-like single crystals were collected by washing with deionized water.

X-ray diffraction (XRD) patterns were measured using a Bruker D8 ADVANCE diffractometer with $\text{Cu K}\alpha$ ($\lambda = 1.5418$ Å) radiation at room temperature. The single-crystal X-ray diffraction (SCXRD) data were performed using a Rigaku XtaLAB Synergy diffractometer at room temperature with the $\text{Mo K}\alpha$ ($\lambda = 0.71073$ Å) radiation. The single crystal structure solution was completed using Olex2 [48] and SHELXL [49]. The high-angle annular-dark-field (HAADF) image and annular bright-field (ABF) image were characterized using an ARM-200F (JEOL, Tokyo, Japan) scanning transmission electron microscope (STEM) operated at 200 keV with a CEOS Cs corrector (CEOS GmbH, Heidelberg, Germany) to cope with the probe-forming objective spherical aberration. The magnetic properties were measured using the Quantum Design Magnetic Property Measurement System (MPMS). The specific heat and resistivity were measured using the Quantum Design Physical Property Measurement System (PPMS). The resistivity was also measured using the Cryogen Free Measurement System (CFMS).

Our DFT uses the generalized gradient approximation (GGA) [50, 51] in the form of PBE functional [52], and included spin-orbit coupling, as implemented in the Vienna ab initio Simulation Package (VASP) [53-55]. The energy cutoff of the plane-wave basis is set to 350 eV. The energy convergence criterion in the self-consistent calculations is set to 10^{-6} eV. A $9 \times 9 \times 3$ Γ -centered Monkhorst-Pack k-point mesh is used for the first Brillouin zone sampling. To account for the correlation effects for Gd, we adopted the GGA + U method with the value of $U=1$ eV.

Results and Discussion:

A. Crystal structure: X-ray diffraction and Scanning transmission electron microscope

A series of (0, 0, 2L) peaks are observed by XRD diffraction experiment in Fig. 1(b), indicating the *ab* plane as the natural cleavage plane. Rocking curve analysis of the Bragg peak (008) in the inset of Fig. 1(b) demonstrates a narrow full-width-at-half-maximum (FWHM) of 0.17° , indicating high quality of the GdZn_3P_3 crystals. The single crystal diffraction spots along [001] in Fig. 1(d) show direct evidence for the six-degree symmetry of hexagonal GdZn_3P_3 system, with related spots along [100] and [010] shown in Fig. S4 [47]. The Rietveld refinements of the SCXRD data converge to the agreement factors $R_1=3.61\%$ and $wR_2=8.96\%$ in Fig. 1(c), with $a = b = 4.0107(3)$ Å and $c = 19.8808(15)$ Å in Table 1. And the corresponding crystal structure is depicted in Fig. 2(c), with the refined atomic parameters listed in Table 2.

Due to the presence of large voids above and below the location in Fig. 2(c), Zn_{trig} atom exhibits large anisotropic displacement parameters, with $U_{33} = 0.048$ along *c*-axis and $U_{11} = 0.032$ in *ab*-plane at room temperature. These values are comparable to the values of 0.0501 and 0.02826 for Cd_{trig} atom of PrCd_3P_3 . On the other hand, the P_{trig} atom has larger in-plane displacement with U_{11} parameter as 0.031, also comparable with the value of 0.0392 for P_{trig} atom of PrCd_3P_3 . The relatively large anisotropy parameters of Zn_{trig} and P_{trig} for GdZn_3P_3 suggest a tendency toward local frustrated bond order within the ZnP honeycomb plane, as observed in isostructural PrCd_3P_3 [46].

To reveal the dynamic disorder of interlayer atoms in atomic scale, we continue to perform STEM on a *bc*-plane of GdZn_3P_3 about $4 \mu\text{m} \times 3 \mu\text{m}$ area, with details information in Fig.S5 [47, 56]. As shown in Fig.2(a), the selected area electron diffraction (SAED) pattern contains a series of diffraction peaks, such as (001), (002), (003), and (004), etc., and (0-10). Moreover, the HAADF image in Fig. 2(b) directly shows the atomic arrangement in the unit cell of GdZn_3P_3 projected along [100] direction, corresponding to the crystal structure in Fig. 2(c). First, the HAADF image confirms the full occupancy of Zn_{trig} and P_{trig} atom within the ZnP_3 trigonal planar. We conclude that the underlying bond instability of $(\text{ZnP})_{\text{trig}}$ are local characteristics rather than uniform.

Notably, numerous interstitial P atoms are observed in the HAADF image, as indicated by the yellow spheres in Fig. 2(b). Within the honeycomb lattice of Zn_{trig} and P_{trig} atoms, the bond distance is about 2.32 Å; while the distance between Zn_{trig} and P_{tet} atom is 3.29 Å along *c* axis. Thus, the presence of interstitial P atom is closely related with the large voids above and below the location of Zn_{trig} atoms in Fig. 2(c). And we will discuss the effect of interstitial P atoms in electronic transport section later.

B. Magnetic Properties and Magnetic Structure

Magnetic susceptibility $\chi(T)$ measurements of GdZn_3P_3 have been performed under magnetic field along a , a^* , and c axis, showing a clear AFM transition at $T_N = 4.5$ K, as shown in Fig. 3(a-b) and Fig. S6-7 [47]. The $\chi(T)$ curve exhibits no significant difference between a and a^* directions, with its value being about 4 times than that along c axis below T_N . In Fig. S7, The Curie-Weiss law is used to fit the $\chi(T)$ (200-300 K) under 0.05 T yield $\mu_{\text{eff}} = 7.93 \mu_B/\text{Gd}$ in ab -plane, consistent with the value $7.94 \mu_B$. In Fig. 3(a-b), the Curie-Weiss law is used to fit the $\chi(T)$ (15-25 K), which yields $\theta_{\text{cw}} = 5.2$ K for $H//a^*$, indicating ferromagnetic (FM) interaction dominates in the ab -plane, and $\theta_{\text{cw}} = -1$ K for $H//c$, indicating AFM interaction dominates along c axis case. These characteristics suggest the formation of an A-type AFM order, likely with the spin alignment of Gd^{3+} ions lying in the ab -plane below T_N and FM layers stacked antiferromagnetically.

Similarly, the A-type AFM order has also been observed in topological material EuM_2X_2 ($\text{M}=\text{Zn}, \text{Cd}$; $\text{X}=\text{P}, \text{As}$), with T_N at about 23 K in EuZn_2P_2 [35-37, 39, 40] and 9 K in EuCd_2As_2 . The much lower T_N in GdZn_3P_3 is speculated to be largely due to the extra honeycomb nets “ZnP” layer between triangular lattice of Gd atoms, thus weakening the AFM interaction strength. According to the previous literature, the magnetic moments of EuCd_2As_2 and EuZn_2As_2 are determined to be parallel to ab -plane through resonant elastic x-ray scattering (REXS) and neutron diffraction; and the spins of EuZn_2P_2 are canted out of the a - a plane by an angle of about $40^\circ \pm 10^\circ$ and aligned along the [100] direction as confirmed by resonant magnetic x-ray diffraction data [30, 34, 35, 37].

We also note a subtle cusp appears in ab -plane $\chi(T)$ curve at 2.4 K (see Fig.3(a) and Fig. S6), and to capture this feature, Fig. S6(a) displays the temperature derivative of $\chi(T)$ ($d\chi/dT$) as a function of temperature. A modulated magnetic order observed in GdV_6Sn_6 indicates the presence of an incommensurate magnetic order below 5.2 K and a commensurate magnetic order below 3.8 K, as demonstrated by REXS measurements [57, 58]. To clarify the microscopic magnetic structure together with its temperature dependence of GdZn_3P_3 , it seems necessary to conduct REXS and neutron scattering measurements in future.

In addition, the $\chi(T)$ curves at different magnetic fields are measured as shown in Fig. 3(c-d). With the magnetic field increased to 0.6 T for $H//a^*$ and 1.4 T for $H//c$, the AFM transition peak has been completely suppressed to below 1.8 K for $H//a^*$ and 2.5 K for $H//c$. The $\chi(T)$ curves as temperature derivatives for $H//a^*$ and $H//c$ at various magnetic fields are presented (Fig. S8) [47]. As shown in Fig. 3(e-f), the experiment saturated magnetization $M_S \sim 6.7 \mu_B$ for $H//a^*$ and $M_S \sim 6.5 \mu_B$ for $H//c$ at 1.8 K, consistent with the value $7 \mu_B$ for Gd^{3+} ions. From the corresponding dM/dH in Fig. 3(e), these transition behaviors were observed at 0.6 T at 1.8 K and 0.5 T at 3 K under field along a^* axis. Finally, Fig.4 (a-b) depicts the H - T phase diagram constructed by combining the AFM transition peaks under different magnetic fields.

C. Magnetic heat capacity and entropy

Fig. 5 presents the temperature dependence of measured heat capacity C_p curve, which reveals a

sharp transition close to $T_N = 4.5$ K. Above 30 K, the background specific heat of phonon contribution is fitted by $C_{ph} = aT + bT^3 + cT^5 + \dots$ [59]. The magnetic heat capacity C_m is obtained after subtracting phonon contribution. There is still residual magnetic entropy below 1.8 K, so the lower temperature magnetic heat capacity is fitted through the power law $C_m(T) = b \times T^a$ to get $a = 1.16$ as shown in Fig. 5(b), which does not follow the $C_m(T) \sim T^3$ relation observed in the conventional ungapped AFM magnon excitations [60]. By integrating $(C_p - C_{ph})/T$ from 15 K to 0 K, the obtained values of the magnetic entropy S_{mag} are 16.3 J/mol·K, which is 94% of the theoretically maximum magnetic entropy as $R \ln 8$. The heat capacity C_p data below 1.8 K seems necessary to obtain a more accurate power law fitting as well as the integrated S_{mag} value.

D. Electronic band structure DFT calculation and Transport results

Similar to EuCd_2As_2 case [33], GdZn_3P_3 may have three possible A-type AFM structures as shown in Fig. 6(a) with magnetic moments of Gd^{3+} ions along b , c , and x directions. Consistent with the magnetic evidence above, the DFT calculations verify the configuration with the moment aligned along b axis exhibits the lowest free energy. The ground state would be most likely the A-type magnetic structure with Gd moment along b axis. Fig. 6(b) and Fig. S9 display the corresponding band structures with spin-orbit coupling included and Density of states (DOS) plot near the Fermi level, with indirect band gaps from Γ to M as 0.27 eV, 0.28 eV, and 0.26 eV, respectively [47]. This band gap is smaller than that of polycrystalline LaCd_3P_3 (0.75 eV) and NdCd_3P_3 (0.63 eV). Besides, the indirect band gap of EuZn_2P_2 is calculated to be 0.2 eV, and observed as 0.09 eV in the angle-resolved photoemission spectroscopy (ARPES) experiment [37].

Fig. 6(c) illustrates the electrical resistivity of polycrystalline GdZn_3P_3 within the temperature range of 2-300 K, consistent with the semiconducting behavior observed in RCd_3P_3 ($R = \text{La, Ce, and Nd}$) polycrystals. As depicted in inset of Fig. 6(c), the transport gap of GdZn_3P_3 is extracted from a fit to the resistivity data between 250 and 300 K using the thermally activated Arrhenius form $\rho = \rho_0 e^{E_{ac}/2k_B T}$, yielding a band gap of approximately 0.2 eV, consistent with the DFT calculation results above. Interestingly, the AFM transition also shows up in the resistivity curve, marked as $T_N = 4.5$ K in Fig. 6(c). A similar characteristic has also been observed in EuZn_2P_2 and EuCd_2As_2 [21, 51].

As shown in inset of Fig. 6(d), the magnetoresistance (MR) curve below 20 K exhibits an initial increase under small field ($H < 0.3$ T), which may be associated with the impurity carriers, similar behavior also reported in EuZn_2As_2 [38]. Under high field, the magnetic scattering would be suppressed in polarized FM state, thus a negative MR has been observed in polycrystalline GdZn_3P_3 under field up to 12 T. According to Fig. 3(e-f), the GdZn_3P_3 compound enters the polarized state under 1 T for $H//a^*$ and 4 T for $H//c$. Thus, the negative MR below 5 K quickly reaches a magnitude of -60% under 4 T, then saturates at this value under $H > 4$ T. The magnitude of negative MR in GdZn_3P_3 is compared to that of EuZn_2As_2 [38], EuZn_2P_2 and EuCd_2As_2 [21, 49]. The MR curve becomes more pronounced as temperature decreases from 20 K to 2 K, indicating the significant influence of magnetic ordering behavior on the electronic transport properties in GdZn_3P_3 .

Fig. 6(e) illustrates the resistivity curve of GdZn_3P_3 single crystal between 2-35 K, exhibiting

metallic behavior with an AFM transition peak around $T_N = 4.5$ K. The resistivity value herein is on the order of 1 m Ω -cm, smaller than the value of 10 m Ω -cm, reported for GdZn₃P₃ single crystal in Ref. [28]. The emergence of metallic conductivity seems closely related with the presence of interstitial P atoms above and below the ZnP honeycomb lattice, revealed by the STEM experiment mentioned above. And the different resistivity value might be caused by the different density of interstitial P atom in this study. Through the RKKY exchange interaction, the charge carrier could also influence the magnetic property. Correspondingly, the value of $\chi(T)$ here is about 2 times than that in Ref. [28] under H//*ab* plane below $T_N = 4.5$ K.

Discussion and Conclusion:

For the magnetic topological system EuMnSb₂ [61-63] and EuCd₂As₂ [32], both materials exhibit narrow-gap semiconductor behavior. The presence of vacancies at Eu sites can introduce hole-type charge carriers and lead to metallic conductivity within the system. Concurrently, the enhanced RKKY interaction between the Eu magnetic moments and these charge carriers slightly alter the temperature-dependent magnetic ordering behavior, resulting in modifications to the spin configuration in the ground-state.

According to ref. [44], the RCd₃P₃ would be semiconductor with band gap between 0.6-0.8 eV, verified by the DFT calculation and the polycrystal results. Given the narrow band gap of the RCd₃P₃ family, these compounds are likely dopable into a metallic state as well. During previous research, single crystals of RCd₃X₃ (R=La, Ce; X=P, As) exhibits metallic behavior, with the resistivity on the order of 10 m Ω -cm (1 m Ω -cm) for P (As) compounds [42, 43]. Based on the Hall effect measurements, the hole-type carrier density in CeCd₃P₃ (CeCd₃As₃) is estimated to be 0.002 (0.003) carriers per formula unit (f.u.) [42, 43]; however, the exact origin remains unclear.

Here, the ZnP bond instability in GdZn₃P₃ has been demonstrated through both X-ray diffraction and STEM measurement. Our atomic resolution STEM measurement reveals the presence of interstitial P atoms close to the ZnP honeycomb lattice, which would cause hole-doping into the GdZn₃P₃ single crystal. Our investigation gives an important insight into the metallic behavior of RZn₃P₃ and RCd₃X₃ (R=La, Ce; X=P, As) single crystals, thus it would be interesting to conduct the STEM measurement on the above single crystal to reveal its origin in atomic scale.

As mentioned above, the local bond instability in ZnP layer could influence the rare-earth magnetic ion triangular layer through the charge carrier mediated RKKY magnetic interaction as observed in GdZn₃P₃; meanwhile, the influence could also be realized through the crystal electronic field (CEF) effect for rare-earth magnetic ion with orbital moment such as in RZn₃P₃ (R=Ce, Pr, Nd, and Sm) system, which deserves further investigation in future. In summary, given the relatively high AFM transition at $T_N = 4.5$ K, the metallic GdZn₃P₃ single crystal opens the possibility of investigating the interplay between short-range bond order and triangular lattice magnetism in two-dimensional RM₃X₃ compounds.

References:

- [1] L. Balents. Spin liquids in frustrated magnets. *Nature* 464, 199 (2010).
- [2] C. Broholm, R. J. Cava, S. A. Kivelson, D. G. Nocera, M. R. Norman, and T. Senthil. Quantum spin liquids. *Science* 367, eaay0668 (2020).
- [3] Y. Li, G. Chen, W. Tong, L. Pi, J. Liu, Z. Yang, X. Wang, and Q. Zhang. Rare-Earth Triangular Lattice Spin Liquid: A Single-Crystal Study of YbMgGaO_4 . *Phys. Rev. Lett.* 115, 167203 (2015).
- [4] Y. Li, D. Adroja, P. K. Biswas, P. J. Baker, Q. Zhang, J. Liu, A. A. Tsirlin, P. Gegenwart, and Q. Zhang. Muon Spin Relaxation Evidence for the U(1) Quantum Spin-Liquid Ground State in the Triangular Antiferromagnet YbMgGaO_4 . *Phys. Rev. Lett.* 117, 097201 (2016).
- [5] J. A. M. Paddison, M. Daum, Z. Dun, G. Ehlers, Y. Liu, Matthew B. Stone, H. Zhou, and M. Mourigal. Continuous excitations of the triangular-lattice quantum spin liquid YbMgGaO_4 . *Nat. Phys.* 13, 117 (2016).
- [6] Y. Shen, Y.-D. Li, H. Wo, Y. Li, S. Shen, B. Pan, Q. Wang, H. C. Walker, P. Steffens, M. Boehm, Y. Hao, D. L. Quintero-Castro, L. W. Harriger, M. D. Frontzek, L. Hao, S. Meng, Q. Zhang, G. Chen, and J. Zhao. Evidence for a spinon Fermi surface in a triangular-lattice quantum-spin-liquid candidate. *Nature* 540, 559 (2016).
- [7] Y. Li, D. Adroja, D. Voneshen, R. I. Bewley, Q. Zhang, A. A. Tsirlin, and P. Gegenwart. Nearest-neighbour resonating valence bonds in YbMgGaO_4 . *Nat. Commun.* 8, 15814 (2017).
- [8] Y. Li, S. Bachus, B. Liu, I. Radelytskyi, A. Bertin, A. Schneidewind, Y. Tokiwa, A. A. Tsirlin, and P. Gegenwart. Rearrangement of Uncorrelated Valence Bonds Evidenced by Low-Energy Spin Excitations in YbMgGaO_4 . *Phys. Rev. Lett.* 122, 137201 (2019).
- [9] C. Castelnovo, R. Moessner, and S. L. Sondhi. Magnetic monopoles in spin ice. *Nature* 451, 42 (2008).
- [10] D. J. P. Morris, D. A. Tennant, S. A. Grigera, B. Klemke, C. Castelnovo, R. Moessner, C. Czternasty, M. Meissner, K. C. Rule, J.-U. Hoffmann, K. Kiefer, S. Gerischer, D. Slobinsky, and R. S. Perry. Dirac Strings and Magnetic Monopoles in the Spin Ice $\text{Dy}_2\text{Ti}_2\text{O}_7$. *Science* 326, 411 (2009).
- [11] T. Fennell, P. P. Deen, A. R. Wildes, K. Schmalzl, D. Prabhakaran, A. T. Boothroyd, R. J. Aldus, D. F. McMorrow, and S. T. Bramwell. Magnetic Coulomb Phase in the Spin Ice $\text{Ho}_2\text{Ti}_2\text{O}_7$. *Science* 326, 415 (2009).
- [12] G. Möller, and R. Moessner. Magnetic multipole analysis of kagome and artificial spin-ice dipolar arrays. *Phys. Rev. B* 80, 140409(R) (2009).
- [13] G.-W. Chern, P. Mellado, and O. Tchernyshyov. Two-Stage Ordering of Spins in Dipolar Spin Ice on the Kagome Lattice. *Phys. Rev. Lett.* 106, 207202 (2011).
- [14] K. Zhao, H. Deng, H. Chen, K. A. Ross, V. Petricek, G. Günther, M. Russina, V. Hutanu, and P. Gegenwart. Realization of the kagome spin ice state in a frustrated intermetallic compound. *Science* 367, 1218 (2020).
- [15] K. Zhao, Y. Tokiwa, H. Chen, and P. Gegenwart. Discrete degeneracies distinguished by the anomalous Hall effect in a metallic kagome ice compound. *Nat. Phys.* 20, 442 (2024).
- [16] K. Zhao, H. Deng, H. Chen, N. Ma, N. Oefele, J. Guo, X. Cui, C. Tang, M. J. Gutmann, T. Mueller, Y. Su, V. Hutanu, C. Jin, and P. Gegenwart. Nonlinear time-reversal symmetry breaking in kagome spin ice HoAgGe . *arXiv:2505.22544*
- [17] Y. Gao, Y.-C. Fan, H. Li, F. Yang, X.-T. Zeng, X.-L. Sheng, R. Zhong, Y. Qi, Y. Wan, and W. Li. Spin supersolidity in nearly ideal easy-axis triangular quantum antiferromagnet $\text{Na}_2\text{BaCo}(\text{PO}_4)_2$.

npj Quantum Mater. 7, 89 (2022).

- [18] J. Xiang, C. Zhang, Y. Gao, W. Schmidt, K. Schmalzl, C.-W. Wang, B. Li, N. Xi, X.-Y. Liu, H. Jin, G. Li, J. Shen, Z. Chen, Y. Qi, Y. Wan, W. Jin, W. Li, P. Sun, and G. Su. Giant magnetocaloric effect in spin supersolid candidate $\text{Na}_2\text{BaCo}(\text{PO}_4)_2$. *Nature* 625, 270 (2024).
- [19] Y. Gao, C. Zhang, J. Xiang, D. Yu, X. Lu, P. Sun, W. Jin, G. Su, and W. Li. Double magnon-roton excitations in the triangular-lattice spin supersolid. *Phys. Rev. B* 110, 214408 (2024).
- [20] J. Sheng, L. Wang, W. Jiang, H. Ge, N. Zhao, T. Li, M. Kofu, D. Yu, W. Zhu, J.-W. Mei, Z. Wang, and L. Wu. Continuum of spin excitations in an ordered magnet. *The Innovation* 6, 100769 (2025).
- [21] W. Liu, Z. Zhang, J. Ji, Y. Liu, J. Li, X. Wang, H. Lei, G. Chen, and Q. Zhang. Rare-Earth Chalcogenides: A Large Family of Triangular Lattice Spin Liquid Candidates. *Chin. Phys. Lett.* 35, 117501 (2018).
- [22] J. Xing, L. D. Sanjeeva, J. Kim, W. R. Meier, A. F. May, Q. Zheng, R. Custelcean, G. R. Stewart, and A. S. Sefat. Synthesis, magnetization, and heat capacity of triangular lattice materials NaErSe_2 and KErSe_2 . *Phys. Rev. Mater.* 3, 114413 (2019).
- [23] P.-L. Dai, G. Zhang, Y. Xie, C. Duan, Y. Gao, Z. Zhu, E. Feng, Z. Tao, C.-L. Huang, H. Cao, A. Podlesnyak, G. E. Granroth, M. S. Everett, J. C. Neufeind, D. Voneshen, S. Wang, G. Tan, E. Morosan, X. Wang, H.-Q. Lin, L. Shu, G. Chen, Y. Guo, X. Lu, and P. Dai. Spinon Fermi Surface Spin Liquid in a Triangular Lattice Antiferromagnet NaYbSe_2 . *Physical Review X* 11, 021044 (2021).
- [24] S. Zheng, H. Wo, Y. Gu, R. L. Luo, Y. Gu, Y. Zhu, P. Steffens, M. Boehm, Q. Wang, G. Chen, and J. Zhao. Exchange-renormalized crystal field excitations in the quantum Ising magnet KTmSe_2 . *Phys. Rev. B* 108, 054435 (2023).
- [25] A. T. Nientiedt, and W. Jeitschko. The Series of Rare Earth Zinc Phosphides RZn_3P_3 ($\text{R}=\text{Y, La-Nd, Sm, Gd-Er}$) and the Corresponding Cadmium Compound PrCd_3P_3 . *J. Solid State Chem.* 146, 478 (1999).
- [26] S. S. Stoyko, and A. Mar. Ternary Rare-Earth Arsenides REZn_3As_3 ($\text{RE} = \text{La-Nd, Sm}$) and RECd_3As_3 ($\text{RE} = \text{La-Pr}$). *Inorg. Chem.* 50, 11152 (2011).
- [27] Y.-D. Li, X. Wang, and G. Chen. Anisotropic spin model of strong spin-orbit-coupled triangular antiferromagnets. *Phys. Rev. B* 94, 035107 (2016).
- [28] N. Kabeya, T. Sakamoto, K. Hara, Y. Hara, S. Nakamura, K. Katoh, and A. Ochiai. Competing Exchange Interactions in Lanthanide Triangular Lattice Compounds LnZn_3P_3 ($\text{Ln} = \text{La-Nd, Sm, Gd}$). *J. Phys. Soc. Jpn.* 89, 074707 (2020).
- [29] K. E. Avers, P. A. Maksimov, P. F. S. Rosa, S. M. Thomas, J. D. Thompson, W. P. Halperin, R. Movshovich, and A. L. Chernyshev. Fingerprinting triangular-lattice antiferromagnet by excitation gaps. *Phys. Rev. B* 103, L180406 (2021).
- [30] M. C. Rahn, J. R. Soh, S. Francoual, L. S. I. Veiga, J. Stremper, J. Mardegan, D. Y. Yan, Y. F. Guo, Y. G. Shi, and A. T. Boothroyd. Coupling of magnetic order and charge transport in the candidate Dirac semimetal EuCd_2As_2 . *Phys. Rev. B* 97, 214422 (2018).
- [31] J. R. Soh, F. de Juan, M. G. Vergniory, N. B. M. Schröter, M. C. Rahn, D. Y. Yan, J. Jiang, M. Bristow, P. A. Reiss, J. N. Blandy, Y. F. Guo, Y. G. Shi, T. K. Kim, A. McCollam, S. H. Simon, Y. Chen, A. I. Coldea, and A. T. Boothroyd. Ideal Weyl semimetal induced by magnetic exchange. *Phys. Rev. B* 100, 201102(R) (2019).
- [32] N. H. Jo, B. Kuthanazhi, Y. Wu, E. Timmons, T.-H. Kim, L. Zhou, L.-L. Wang, B. G. Ueland, A. Palasyuk, D. H. Ryan, R. J. McQueeney, K. Lee, B. Schunk, A. A. Burkov, R. Prozorov, S. L.

- Bud'ko, A. Kaminski, and P. C. Canfield. Manipulating magnetism in the topological semimetal EuCd_2As_2 . *Phys. Rev. B* 101, 140402(R) (2020).
- [33] Y. Wang, C. Li, Y. Li, X. Zhou, W. Wu, R. Yu, J. Zhao, C. Yin, Y. Shi, C. Jin, J. Luo, L. Zhao, T. Xiang, G. Liu, and X. J. Zhou. Long-Time Magnetic Relaxation in Antiferromagnetic Topological Material EuCd_2As_2 . *Chin. Phys. Lett.* 38, 077201 (2021).
- [34] Z.-C. Wang, E. Been, J. Gaudet, G. M. A. Alqasseri, K. Fruhling, X. Yao, U. Stuhr, Q. Zhu, Z. Ren, Y. Cui, C. Jia, B. Moritz, S. Chowdhury, T. Devereaux, and F. Tafti. Anisotropy of the magnetic and transport properties of EuZn_2P_2 . *Phys. Rev. B* 105, 165122 (2022).
- [35] T. Berry, V. J. Stewart, B. W. Y. Redemann, C. Lygouras, N. Varnava, D. Vanderbilt, and T. M. McQueen. A-type antiferromagnetic order in the Zintl-phase insulator EuZn_2P_2 . *Phys. Rev. B* 106, 054420 (2022).
- [36] K. Singh, S. Dan, A. Ptok, T. A. Zaleski, O. Pavlosiuk, P. Wiśniewski, and D. Kaczorowski. Superexchange interaction in insulating EuZn_2P_2 . *Phys. Rev. B* 108, 054402 (2023).
- [37] S. Krebber, M. Kopp, C. Garg, K. Kummer, J. Sichelschmidt, S. Schulz, G. Poelchen, M. Mende, A. V. Virovets, K. Warawa, M. D. Thomson, A. V. Tarasov, D. Y. Usachov, D. V. Vyalikh, H. G. Roskos, J. Müller, C. Krellner, and K. Kliemt. Colossal magnetoresistance in EuZn_2P_2 and its electronic and magnetic structure. *Phys. Rev. B* 108, 045116 (2023).
- [38] S. Luo, Y. Xu, F. Du, L. Yang, Y. Chen, C. Cao, Y. Song, and H. Yuan. Colossal magnetoresistance and topological phase transition in EuZn_2As_2 . *Phys. Rev. B* 108, 205140 (2023).
- [39] X. Chen, W. Yang, J.-Y. Lu, Z. Zhou, Z. Ren, G.-H. Cao, S. Dong, and Z.-C. Wang. Carrier-induced transition from antiferromagnetic insulator to ferromagnetic metal in the layered phosphide EuZn_2P_2 . *Phys. Rev. B* 109, L180410 (2024).
- [40] D. Rybicki, K. Komędera, J. Przewoźnik, Ł. Gondek, C. Kapusta, K. Podgórska, W. Tabiś, J. Żukrowski, L. M. Tran, M. Babij, Z. Bukowski, L. Havela, V. Buturlim, J. Prchal, M. Divis, P. Kral, I. Turek, I. Halevy, J. Kastil, M. Misek, U. Dutta, and D. Legut. Ambient- and high-pressure studies of structural, electronic, and magnetic properties of single-crystal EuZn_2P_2 . *Phys. Rev. B* 110, 014421 (2024).
- [41] O. P. Uzoh, S. Kim, and E. Mun. Influence of crystalline electric field on the magnetic properties of CeCd_3X_3 ($\text{X} = \text{P}, \text{As}$). *Phys. Rev. Mater.* 7, 013402 (2023).
- [42] J. Lee, A. Rabus, N. R. Lee-Hone, D. M. Broun, and E. Mun. The two-dimensional metallic triangular lattice antiferromagnet CeCd_3P_3 . *Phys. Rev. B* 99, 245159 (2019).
- [43] S. R. Dunsiger, J. Lee, J. E. Sonier, and E. D. Mun. Long-range magnetic order in the anisotropic triangular lattice system CeCd_3As_3 . *Phys. Rev. B* 102, 064405 (2020).
- [44] J. R. Chamorro, A. R. Jackson, A. K. Watkins, R. Seshadri, and S. D. Wilson. Magnetic order in the $S_{\text{eff}}=1/2$ triangular-lattice compound NdCd_3P_3 . *Phys. Rev. Mater.* 7, 094402 (2023).
- [45] A. Ochiai, N. Kabeya, K. Maniwa, M. Saito, S. Nakamura, and K. Katoh. Field-induced anomalous magnetic state beyond the magnetically ordered state in the slightly distorted triangular $S=1/2$ rare-earth antiferromagnet CeZn_3P_3 . *Phys. Rev. B* 104, 144420 (2021).
- [46] S. J. G. Alvarado, J. R. Chamorro, A. R. Jackson, G. Pokharel, R. Gomez, B. R. Ortiz, S. Sarker, L. Kautzsch, L. C. Gallington, R. Seshadri, and Stephen D. Wilson. Interleaved bond and magnetic frustration in triangular lattice LnCd_3P_3 . *arXiv:2501.04203v1*
- [47] See Supplemental Material for additional details about X-ray diffraction, Magnetization, and DFT results.
- [48] O. V. Dolomanov, L. J. Bourhis, R. J. Gildea, J. A. K. Howard, and H. Puschmann. OLEX2: a

- complete structure solution, refinement and analysis program. *J. Appl. Crystallogr.* 42, 339 (2009).
- [49] G. M. Sheldrick. A short history of SHELX. *Acta Crystallogr., Sect. A: Found. Crystallogr.* 64, 112 (2007).
- [50] A. D. Becke. Density-functional exchange-energy approximation with correct asymptotic behavior. *Phys. Rev. A* 38, 3098 (1988).
- [51] J. P. Perdew, J. A. Chevary, S. H. Vosko, K. A. Jackson, M. R. Pederson, D. J. Singh, and C. Fiolhais. Atoms, molecules, solids, and surfaces: Applications of the generalized gradient approximation for exchange and correlation. *Phys. Rev. B* 46, 6671 (1992).
- [52] J. P. Perdew, K. Burke, and M. Ernzerhof. Generalized Gradient Approximation Made Simple. *Phys. Rev. Lett.* 77, 3865 (1996).
- [53] G. Kresse, and J. Hafner. Ab initio molecular dynamics for liquid metals. *Phys. Rev. B* 47, 558 (1993).
- [54] G. Kresse, and J. Furthmüller. Efficiency of ab-initio total energy calculations for metals and semiconductors using a plane-wave basis set. *Comput. Mater. Sci.* 6, 15 (1996).
- [55] G. Kresse, and J. Furthmüller. Efficient iterative schemes for ab initio total-energy calculations using a plane-wave basis set. *Phys. Rev. B* 54, 11169 (1996).
- [56] K. Zhao, E. Golias, Q. H. Zhang, M. Krivenkov, A. Jesche, L. Gu, O. Rader, I. I. Mazin, and P. Gegenwart. Quantum oscillations and Dirac dispersion in the BaZnBi₂ semimetal guaranteed by local Zn vacancy order. *Phys. Rev. B* 97, 115166 (2018).
- [57] G. Pokharel, S. M. L. Teicher, B. R. Ortiz, P. M. Sarte, G. Wu, S. Peng, J. He, R. Seshadri, and S. D. Wilson. Electronic properties of the topological kagome metals YV₆Sn₆ and GdV₆Sn₆. *Phys. Rev. B* 104, 235139 (2021).
- [58] Z. Porter, G. Pokharel, J.-W. Kim, P. J. Ryan, and S. D. Wilson. Incommensurate magnetic order in the Z₂ kagome metal GdV₆Sn₆. *Phys. Rev. B* 108, 035134 (2023).
- [59] Z. Y. Yang, H. H. Zhang, M. J. Bai, W. Li, S. L. Huang, S. C. Ruan, and Y. J. Zeng. Large magnetocaloric effect in gadolinium borotungstate Gd₃BWO₉. *J. Mater. Chem. C* 8, 11866 (2020).
- [60] Z. W. Yang, J. Zhang, B. Liu, X. Zhang, D. Lu, H. Zhao, M. Pi, H. Cui, Y. J. Zeng, Z. Pan, Y. Shen, S. Li, and Y. Long. Exceptional Magnetocaloric Responses in a Gadolinium Silicate with Strongly Correlated Spin Disorder for Sub-Kelvin Magnetic Cooling. *Adv. Sci.* 11, 2306842 (2024).
- [61] L. Zhang, Z. Sun, A. Wang, Y. Xia, X. Mi, L. Zhang, M. He, Y. Chai, T. Wu, R. Wang, X. Zhou, and X. Chen. Strong coupling between magnetic order and band topology in the antiferromagnet EuMnSb₂. *Phys. Rev. B* 104, 205108 (2021).
- [62] J. M. Wilde, S. X. M. Riberolles, A. Das, Y. Liu, T. W. Heitmann, X. Wang, W. E. Straszheim, S. L. Bud'ko, P. C. Canfield, A. Kreyssig, R. J. McQueeney, D. H. Ryan, and B. G. Ueland. Canted antiferromagnetic phases in the candidate layered Weyl material EuMnSb₂. *Phys. Rev. B* 106, 024420 (2022).
- [63] K. Zhao, X. Chen, Z. Wang, J. Liu, J. Wu, C. Xi, X. Lv, L. Li, Z. Zhong, and P. Gegenwart. Magnetic tuning of band topology evidenced by exotic quantum oscillations in the Dirac semimetal EuMnSb₂. *Phys. Rev. B* 107, L081112 (2023).

Acknowledgements

The authors would like to thank Peijie Sun, Junsen Xiang, Jiabing Xiang, Huifen Ren, Tao Sun and Shaokui Su for helpful discussions and experimental support. The work was supported by the Beijing Natural Science Foundation (Grant No. JQ24012), National Key R&D Program of China (Grant No. 2023YFA1406003, 2022YFA1402600, 2023YFA1406300 and 2024YFA1409500), National Natural Science Foundation of China (Grants No. 12274015, 12174018 and 52322212), and the Fundamental Research Funds for the Central Universities. The authors acknowledge the facilities, and the scientific and technical assistance of the Analysis & Testing Center, Beihang University. A portion of this work was carried out at the Synergetic Extreme Condition User Facility (SECUF).

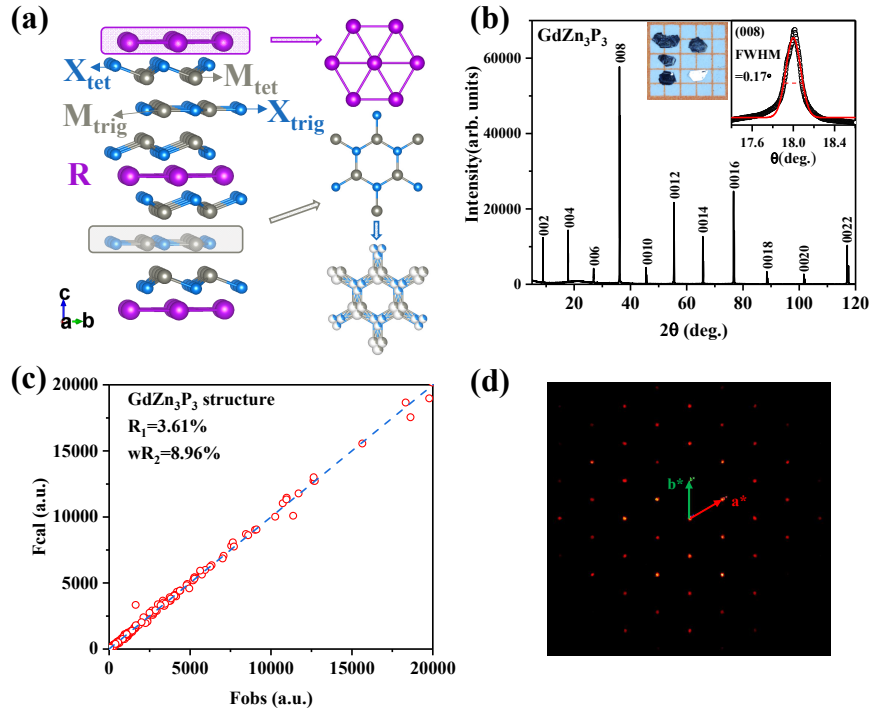


Fig. 1. (a) The crystal structure of RM_3X_3 (R =rare earth; M =Zn, Cd; X =P, As), with space group $P6_3/mmc$. Purple, grey, and blue spheres represent R, M, and X atoms, respectively. The triangular layer formed by R ions. The honeycomb network formed by MX_3 trigonal planar units, which M_{trig} and X_{trig} occupy 1, to the local distorted arrangement in which M_{trig} and X_{trig} are randomly distributed over three equivalent positions, respectively. (b) The XRD pattern of the $GdZn_3P_3$ single crystal, with the inset illustrating the Rocking curve scan of the (008) peak fitted by Gaussian function, and a photograph of the single crystals also included. (c) Plots of calculated vs experimental structure factors for the refined structure at room temperature. (d) The diffraction spot pattern taken looking along the [001] from the single-crystal X-ray diffraction of $GdZn_3P_3$.

Table 1. Crystal data and structure refinement
for single-crystal GdZn₃P₃.

Formula	GdZn ₃ P ₃
T(K)	293(2)
Crystal system	Hexagonal
Space group	P6 ₃ /mmc
a(Å)	4.0107(3)
b(Å)	4.0107(3)
c(Å)	19.8808(15)
V(Å) ³	276.95(4)
θ	2.049-28.158
No. reflections collected	1066
No. of variables	14
Final R indices	R ₁ =0.0361, wR ₂ =0.0896
R indices (all data)	R ₁ =0.0405, wR ₂ =0.0911
Goodness of fit	0.992
Largest diff. peak and hole(eÅ ⁻³)	0.92, -1.09

Table 2. Wyckoff positions, atomic coordinates, occupancies, isotropic and anisotropic displacement parameters (Å²), where $U_{23}=U_{13}=0$ for GdZn₃P₃.

Atom.	Wyck.	x	y	z	Occu.	U(eq)	U ₁₁ (U ₂₂)	U ₃₃	U ₁₂
Gd	2a	0	0	0.5	1	0.0095(5)	0.0075(6)	0.0134(8)	0.0038(3)
Zn _{tet}	4f	-1/3	1/3	0.6299(1)	1	0.0136(7)	0.0139(9)	0.0130(11)	0.0069(5)
Zn _{trig}	2d	-2/3	2/3	3/4	1	0.0374(13)	0.0321(19)	0.048(3)	0.0160(9)
P _{tet}	4f	2/3	1/3	0.4155(3)	1	0.0112(12)	0.0117(17)	0.010(2)	0.0058(8)
P _{trig}	2c	-1/3	1/3	3/4	1	0.024(2)	0.031(4)	0.011(4)	0.0153(18)

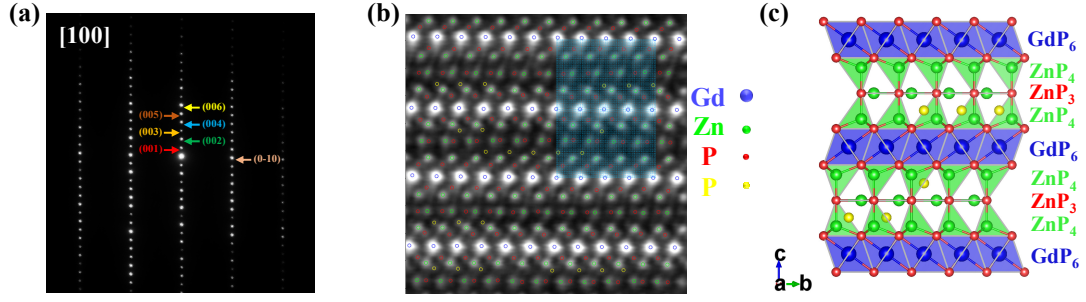


Fig. 2. (a) The electron diffraction pattern along [100] direction. (b) The high-angle annular dark-field (HAADF) image of GdZn₃P₃ taken along [100] direction. The blue, green, red, and yellow spheres represent Gd, Zn, P, and the interstitial impurity P, respectively. (c) Corresponding crystal structure of GdZn₃P₃ along [100] direction, matching the blue-boxed region in Fig. 2(b). The structure features alternating layers of GdP₆ octahedra, ZnP₄ tetrahedra, and ZnP₃ trigonal planar units, with the red ball marks the anticipated site of the interstitial P atom.

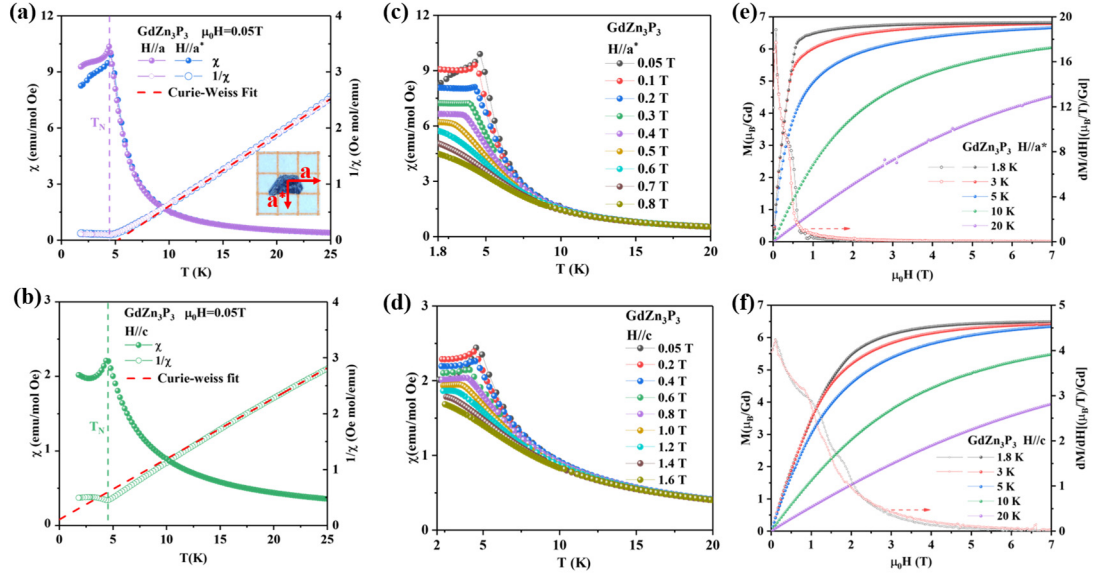


Fig. 3. (a, b) The temperature-dependent magnetic susceptibility $\chi(T)$ of GdZn_3P_3 between 1.8 and 25 K measured with magnetic field along a , a^* and c directions, an inset optical image of the single crystal. (c, d) The $\chi(T)$ below 20 K at various fields along a^* and c directions. (e, f) Isothermal magnetization and the differential susceptibility dM/dH at different temperatures with the magnetic field applied along the a^* and c directions.

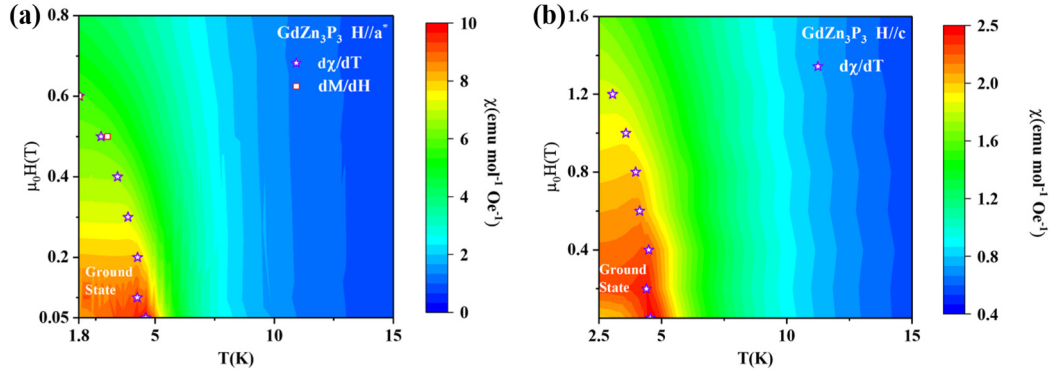


Fig. 4. (a, b) The H - T magnetic phase diagram overlaid on the contour plots of the magnetic susceptibility of GdZn_3P_3 with the field along the a^* and c directions, respectively. The magnetic phase boundaries were extracted through $\chi(T)$ and $M(H)$ measurements. The star and square symbols respectively denote the temperature at a specific field where these transition peaks observed in the temperature derivative of susceptibility $d\chi/dT$ and the differential susceptibility dM/dH .

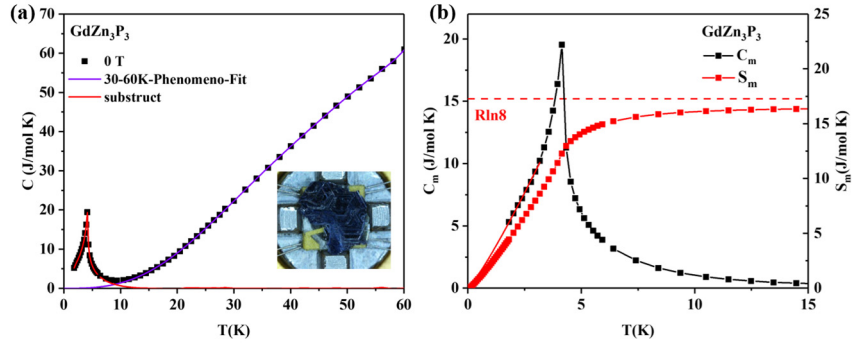


Fig. 5. (a) Temperature-dependent Specific-heat (black square) of GdZn_3P_3 in zero field, temperature dependence of the magnetic specific heat $C_m(T)$ (red line) with the phonon contribution (purple line) removed, and an inset photo of the single crystal for heat capacity measurement in the PPMS puck. (b) The C_m (black line) with the portion of the zero field $C_m(T)$ fitted to a $b \times T^a$ power law (red extension line) and temperature-dependent integrated magnetic entropy (red line).

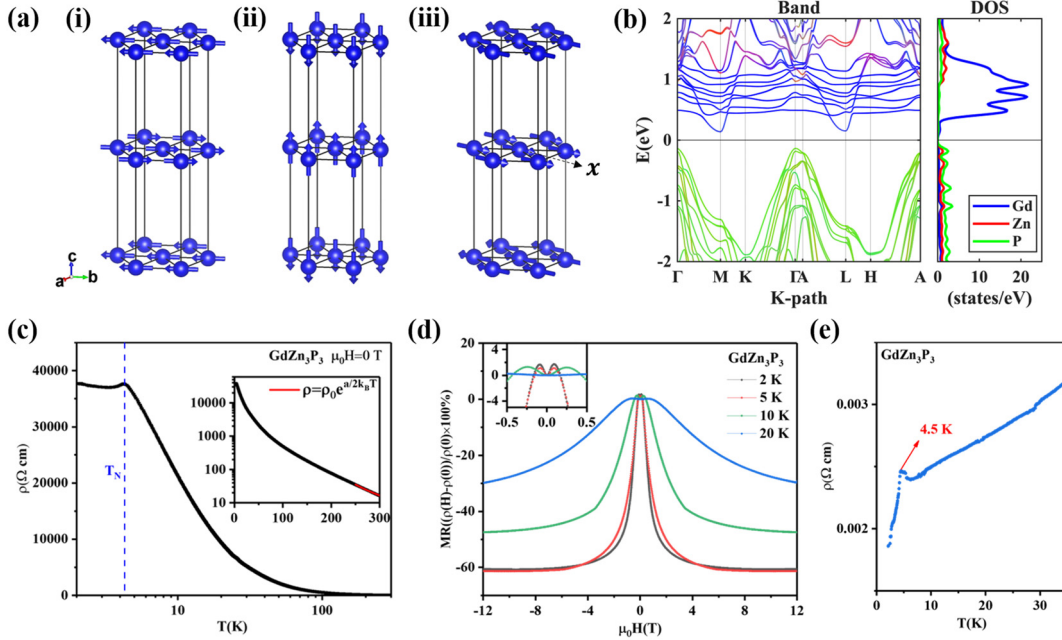


Fig. 6. (a) Proposed possible magnetic structure of GdZn_3P_3 . A-type AFM structure configurations on Gd sites with the magnetic moment aligned along b (i), c (ii) or x (iii) directions. (b) (i) corresponding Band structure with spin-orbit coupling included and Density of states (DOS) plot near the Fermi level, calculated via Density functional theory (DFT). (c) The temperature-dependent resistivity of polycrystalline GdZn_3P_3 sample between 2 K and 300 K, with the inset shows the transport activation gap extracted from a fit in the 250-300 K range. (d) Magnetoresistance (MR) of GdZn_3P_3 as a function of field at several representative temperatures, with the inset reveals the detailed behavior of MR in the field range of -0.5 T to 0.5 T. (e) The temperature-dependent resistivity of single crystal GdZn_3P_3 between 1.8 K and 35 K.